

# Optical efficiency of image sensor pixels

Peter B. Catrysse and Brian A. Wandell

*Department of Electrical Engineering, Stanford University, Stanford, California 94305*

Received November 19, 2001; accepted January 31, 2002

The ability to reproduce a high-quality image depends strongly on the image sensor light sensitivity. This sensitivity depends, in turn, on the materials, the circuitry, and the optical properties of the pixel. We calculate the optical efficiency of a complementary metal oxide semiconductor (CMOS) image sensor pixel by using a geometrical-optics phase-space approach. We compare the theoretical predictions with measurements made by using a CMOS digital pixel sensor, and we find them to be in agreement within 3%. Finally, we show how to use these optical efficiency calculations to trade off image sensor pixel sensitivity and functionality as CMOS process technology scales. © 2002 Optical Society of America

*OCIS codes:* 040.5160, 040.6040, 080.2720, 110.2970.

## 1. INTRODUCTION

The ability to reproduce a high-quality image depends strongly on the light sensitivity of an image sensor. Two factors significantly influence light sensitivity. First, the materials (process technology) and the devices (photodetector type) that convert photons to electrons within each image sensor pixel set a limit on light sensitivity. Second, the light sensitivity depends on the geometric arrangement of the photodetector within an image sensor pixel and the pixel location with respect to the imaging optics. The former leads to quantum efficiency (QE), and the latter can be summarized as optical efficiency (OE).

An important figure of merit for an image sensor is the external QE of its pixels. External QE measures the fraction of the incident photon flux that contributes to the photocurrent in the pixel as a function of wavelength; it comprises both QE and OE. Because of its complex dependency on materials and devices, external QE is typically obtained experimentally.<sup>1-3</sup> It is a global figure of merit and gives no detailed information about the nature, i.e., quantum or optical, of an efficiency bottleneck within the pixel. It is possible to characterize the photodetector in a pixel by an internal QE, for which theoretical models exist.<sup>4</sup> Unfortunately, most model assumptions break down for the small photodetectors integrated within typical image sensor pixels. In this paper, however, we will focus on the OE of an image sensor pixel and not elaborate on its internal QE.

Before the photon flux incident on a pixel is converted into a photocurrent, it has to reach the photodetector. We define OE as the photon-to-photon efficiency from the pixel surface to the photodetector. Figure 1 is a scanning electron microscope image of a complementary metal oxide semiconductor (CMOS) image sensor pixel.<sup>5</sup> The image shows a cross section through the pixel; light is incident on the pixel surface, enters at the aperture, passes through several dielectric layers forming a tunnel, and is absorbed by a photodetector on the pixel floor. The geometric arrangement of the photodetector with respect to other elements of the pixel structure, i.e., shape and size of the aperture, length of the dielectric tunnel, and posi-

tion, shape, and size of the photodetector, all determine OE. Experimental evidence shows that OE can be a significant factor when an image sensor pixel is implemented by using either charge-coupled-device (CCD) or CMOS technology.<sup>6,7</sup> Nevertheless, the OE of image sensor pixels has not been separately analyzed within a comprehensive optical framework. Several commercial ray-trace programs include useful simulations that permit inferences about OE.<sup>8,9</sup> These programs rely mainly on brute force calculations, which in most cases have not been validated with the use of appropriate pixel test structures. There is one published description of three-dimensional (3D) CCD modeling, but this study does not present an experimental validation.<sup>10</sup>

In this paper, we develop a theoretical basis for OE calculations by using a geometrical-optics phase-space (PS) approach, and we provide a graphical method of deriving the OE of image sensor pixels. We make specific predictions for the CMOS image sensor pixel shown in Fig. 1, and we validate our model by using experimental measurements. We then extend the predictions for pixels implemented in future CMOS process technologies. The remainder of the paper is organized as follows. In Section 2, we introduce the PS approach and show how it applies to optical signals and systems. In Section 3, we calculate the OE of an imaging system consisting of a lens and an image sensor. In Sections 4 and 5, the experimental measurements are described and compared with the theoretical PS predictions. In Section 6, we show how to use these OE calculations to trade off pixel sensitivity and functionality as CMOS process technology scales.

## 2. THEORETICAL BACKGROUND

### A. Geometrical-Optics Phase Space

Hamilton introduced the PS approach to light propagation in geometrical optics.<sup>11</sup> Winston further developed this approach by introducing PS representations to study light collection.<sup>12</sup> We extend Winston's results in two ways. The initial use of PS representations was to describe optical signals. Here we show that it is possible to use PS representations to describe optical systems as

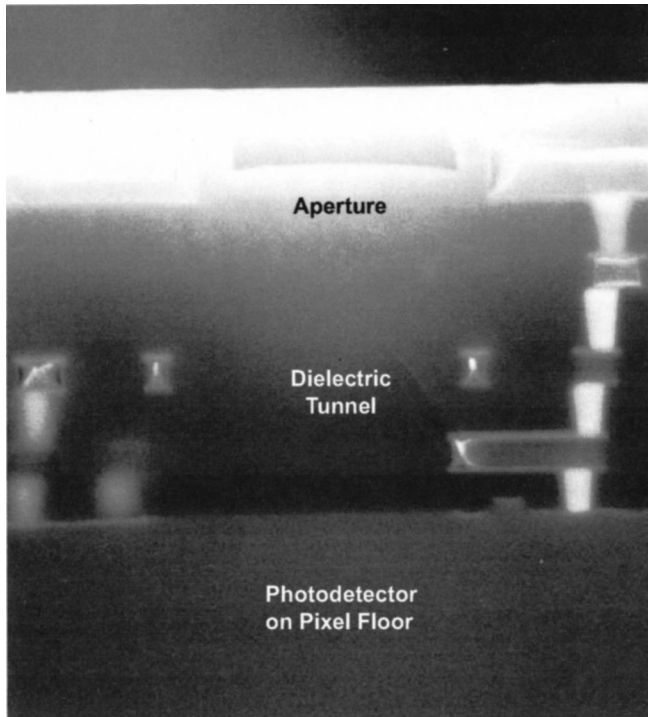


Fig. 1. Scanning electron microscope image of a CMOS image sensor pixel. The image shows a cross section. The white areas show the metal layers and the connection vias. The top white layer is a dielectric passivation layer ( $\text{Si}_3\text{N}_4$ ) sitting on top of a metal light shield. The shield has a square aperture so that incident light can reach the photodetector. The photodetector (Si) is located at the bottom of a dielectric tunnel ( $\text{SiO}_2$ ) of width  $5.5 \mu\text{m}$  and depth  $7.08 \mu\text{m}$ .

well. Second, we show how to combine the signal and system PS representations, predict the system response from the signal–system PS, and determine the system OE.

Geometrical-optics PS representations consist of a four-dimensional (4D) function whose entries describe the relationship between each geometrical light ray and a plane, which is typically perpendicular to the optical axis. Two of the four dimensions define the location of the ray intersection with the plane,  $(x, y)$ ; the other two dimensions describe the angles between the ray and the optical axis at the intersection point,  $(\theta_x, \theta_y)$ . In the geometrical-optics PS representation, these angles are usually measured in terms of  $(p, q)$ , given by

$$p = n \sin \theta_x, \quad q = n \sin \theta_y, \quad (1)$$

where  $n$  is the index of refraction of the material at the plane. We call  $(p, q)$  “generalized reduced angles,” because they are a nonparaxial generalization of the reduced angles defined by Goodman.<sup>13</sup> The spatial dimensions  $(x, y)$  are unbounded; the angular dimensions  $(p, q)$  fall within a range of  $-n$  to  $n$ : i.e., the PS representation is limited to forward-propagating rays.

Two-dimensional (2D) signals and systems  $u(x, y)$ , such as imaging systems, have 4D PS representations  $W(x, y, p, q)$ . In certain cases, the 4D representation can be reduced to a 2D PS representations,  $W(x, p)$ . This dimensionality reduction is possible whenever the 2D system can be represented by a simpler one-

dimensional (1D) system, for example in the case of rotational symmetry. In this case, the position along one spatial dimension  $x_0$  and one angle  $\theta_0$  are enough to characterize each light ray. Figure 2 shows the 2D PS representation of a geometrical ray: a point  $(x_0, p_0)$  in PS, where the generalized reduced angle is  $p_0 = n \sin \theta_0$ . To provide an intuitive explanation of PS representations and their use in determining pixel OE, we will rely on 1D signals and systems  $u(x)$  and a 2D PS representations,  $W(x, p)$ . The geometrical-optics Phase Space Toolbox that we have developed uses the general 4D representation  $W(x, y, p, q)$ .

In general, the relationship between a 1D signal or system  $u(x)$  and its 2D PS representation is obtained by the Wigner transform<sup>14,15</sup>:

$$W(x, \nu) = \int u(x + x'/2)u^*(x - x'/2)\exp(-2\pi i \nu x')dx'. \quad (2)$$

The Wigner transform from  $u(x)$  to  $W(x, \nu)$  is reversible up to a constant phase factor:

$$\int W(x/2, \nu)\exp(2\pi i \nu x)d\nu = u(x)u^*(0),$$

$$|u(0)|^2 = \int W(0, \nu)d\nu. \quad (3)$$

We now define geometrical-optics PS as a binary function of two variables,

$$W_{\text{geom}}(x, p) = \begin{cases} 1 & W(x, \nu) > W_{\text{thresh}} \\ 0 & \text{otherwise} \end{cases}, \quad (4)$$

using a threshold value  $W_{\text{thresh}}$ , and we relate the spatial frequency  $\nu = (n \sin \theta)/\lambda$  to the generalized reduced angle  $p$  by

$$p = \lambda \nu. \quad (5)$$

In what follows, we replace the subscript “geom” in order to distinguish between PS representations of optical signals,  $W_I(x, p)$ , and of optical systems,  $W_Y(x, p)$ .

### 1. Phase-Space Representation of Signals

Consider the PS representations  $W_I(x, p)$  of some fundamental optical signals that can be used as input to an image sensor. A single ray of unit radiance is described by a position  $x_0$  and a direction  $p_0 = n \sin \theta_0$ . We can use the Dirac  $\delta$  to represent the signal as (cf. Fig. 2)

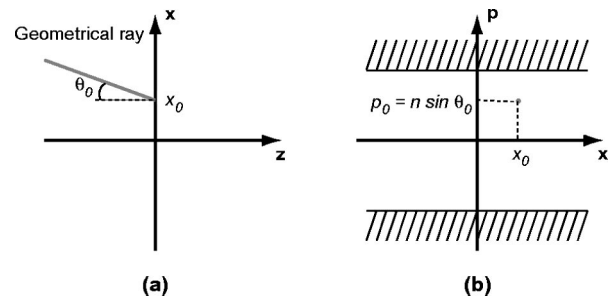


Fig. 2. Geometrical-optics PS: The parameters  $(x_0, p_0)$  define a geometrical ray incident on a surface in (a) one-dimensional real space and (b) two-dimensional phase space.

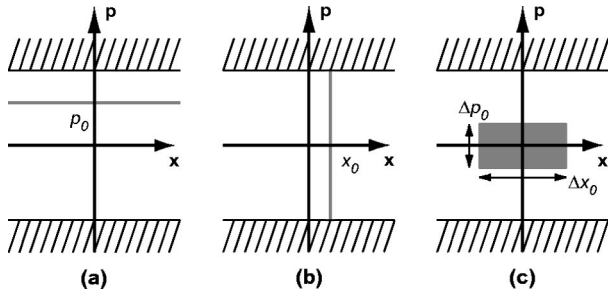


Fig. 3. PS representation of optical signals: (a) plane wave, (b) point source, (c) area source.

$$W_I(x, p) = \delta(x - x_0, p - p_0) = \delta(x - x_0)\delta(p - p_0). \quad (6)$$

A plane wave of unit radiance has a single direction of propagation,  $p_0 = n \sin \theta_0$ , and extends infinitely across space. A horizontal line represents the plane wave in PS [Fig. 3(a)]:

$$W_I(x, p) = \delta(p - p_0). \quad (7)$$

A point source exists at a single position  $x_0$  in space and emits light in all directions. A vertical line represents the point source in PS [Fig. 3(b)]:

$$W_I(x, p) = \delta(x - x_0). \quad (8)$$

An incoherent area source can consist of the image produced by a lens filled with light<sup>16</sup> centered on the spatial axis  $x_0$  in position. The rays are confined in space by the finite diameter of the lens field stop,  $\Delta$ , and confined in angle by the lens numerical aperture (NA). A closed area represents the area source in PS [Fig. 3(c)]:

$$\begin{aligned} W_I(x, p) &= \Pi\left(\frac{x - x_0}{\Delta}, \frac{p - p_0}{2NA}\right) \\ &= \Pi\left(\frac{x - x_0}{\Delta}\right)\Pi\left(\frac{p - p_0}{2NA}\right). \end{aligned} \quad (9)$$

We define  $\Pi$  as the rectangle function<sup>17</sup>:

$$\Pi\left(\frac{x - x_0}{\Delta x_0}\right) = \begin{cases} 1, & x_0 - \frac{\Delta x_0}{2} \leq x \leq x_0 + \frac{\Delta x_0}{2} \\ 0, & \text{else} \end{cases}. \quad (10)$$

Finally, the photon flux of the optical signal is the integral of the geometrical-optics PS representation:

$$\Phi = \iint W_I(x, p) dx dp. \quad (11)$$

## 2. Phase-Space Representation of Systems

PS representations can also be used to describe the acceptance range of signals incident on an optical system. We denote these system representations by  $W_Y(x, p)$ . Here the axes are unchanged from the signal diagram, but the value assigned to each location in the representation defines the system's relative responsivity to a ray at that position and angle. In many applications, it is sufficient to summarize this responsivity by using a binary value, in which we treat each ray as falling either in or out of the system's acceptance range:

$$W_Y(x, p) = \begin{cases} 1 & \text{within acceptance range} \\ 0 & \text{else} \end{cases}. \quad (12)$$

The system's responsivity can now be described graphically by using shaded PS graphs (Fig. 4). As an imaging sensor example, consider the PS representation for a pixel with a surface photodetector located at the pixel aperture plane. Figure 4(a) shows that the horizontal axis of the PS representation spans the pixel width  $w$  and that the vertical axis spans the full hemisphere  $2n$ :

$$W_Y(x, p) = \Pi\left(\frac{x}{w}\right)\Pi\left(\frac{p}{2n}\right). \quad (13)$$

If the photodetector spans only half of the pixel aperture,  $w/2$ , the shaded region shrinks accordingly, as shown in Fig. 4(b):

$$W_Y(x, p) = \Pi\left(\frac{x}{w/2}\right)\Pi\left(\frac{p}{2n}\right). \quad (14)$$

Finally, consider the PS representation of an on-axis pixel at the image plane of a lens [Fig. 4(c)]. The PS representation of the lens-pixel system at the pixel aperture plane depends jointly on the lens and the pixel PS representations [Fig. 4(b)]. The PS representation of the system is necessarily the intersection of the two PS representations. On the horizontal axis, the PS of the lens spans the width of the field stop,  $\Delta$ ; the pixel is bounded by the width  $w/2$  of the photodetector. On the vertical axis, the pixel accepts a full hemisphere; the lens, however, is bounded by its NA:

$$W_Y(x, p) = \Pi\left(\frac{x}{w/2}\right)\Pi\left(\frac{p}{2NA}\right). \quad (15)$$

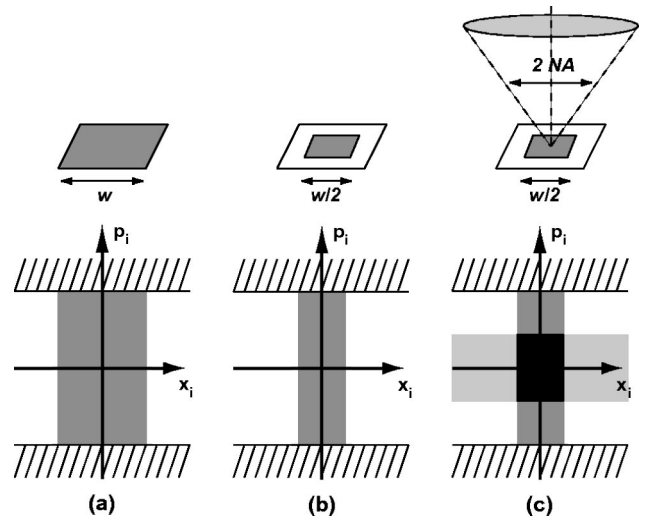


Fig. 4. PS representations of several surface photodetector configurations: (a) photodetector covering the entire pixel area (100% fill factor), (b) photodetector covering half of the pixel area (50% fill factor), (c) photodetector covering half of the pixel area placed on axis in the imaging plane of a lens. The light-shaded area represents the PS representation of the lens at the image plane, and the black rectangle indicates the intersection of the surface photodetector PS and the lens PS.

The integral of the geometrical-optics PS representation measures the geometric etendue  $G$ , i.e., the maximum incident photon flux transmittable by the optical system<sup>18</sup>:

$$G = \iint W_Y(x, p) dx dp. \quad (16)$$

Geometric etendue  $G$  is the energetic equivalent of the optical space–bandwidth product described in Lohmann *et al.*<sup>19</sup> It is a limiting function of system throughput and is determined by the least-optimized segment of the entire system. We now derive the geometric etendue  $G$  for the example image sensor systems in Fig. 4. For a pixel with a surface photodetector spanning the entire pixel width  $w$  in a medium with refractive index  $n$ , the etendue is  $G = 2nw$ . This is the maximum achievable etendue for an image sensor pixel. A more realistic system would consist of a surface photodetector spanning only half of the pixel width and the pixel located on axis in the image plane behind a lens. As a result of a reduction of the PS representation in both  $x$  and  $p$  dimensions, the geometric etendue reduces to  $G = (NA)w$ .

### 3. Combining Signals and Systems

We now define the combined signal–system PS representation, which defines all the angles and the positions of incident signal rays that are accepted by the system:

$$W_{IY}(x, p) = W_I(x, p)W_Y(x, p). \quad (17)$$

The integral of the signal–system PS representation,  $\iint W_{IY}(x, p) dx dp$ , defines an upper bound on the fraction of incident light transmitted by the optical system.

### 4. Phase-Space Transformation: Canonical Planes

To characterize an optical system in PS and to calculate its etendue, we must choose a suitable reference plane that we call the canonical plane. Using a canonical plane simplifies the combining of signal and system PS representations because one can compute quantities in a convenient plane and then refer them to the canonical plane. The procedure of converting the PS representations between planes, when the paraxial approximation is valid, is described by ray-transfer-matrix rules.<sup>20</sup> Each ray in the pixel aperture plane is assigned a corresponding ray at the pixel floor by application of the following ray transfer matrix:

$$\begin{pmatrix} x_o \\ p_o \end{pmatrix} = \begin{bmatrix} A & B \\ C & D \end{bmatrix} \begin{pmatrix} x_i \\ p_i \end{pmatrix}. \quad (18)$$

We typically apply a succession of ray transfer matrices for more complex systems; for a pixel, we apply one for each dielectric layer in the tunnel. In general, the transformation for each layer comprises the product of two matrices, a free-space propagation matrix and an interface transformation matrix. The free-space propagation matrix is

$$\begin{pmatrix} x_o \\ p_o \end{pmatrix} = \begin{bmatrix} 1 & -d/n \\ 0 & 1 \end{bmatrix} \begin{pmatrix} x_i \\ p_i \end{pmatrix}, \quad (19)$$

where  $d$  is the distance of the free-space propagation and  $n$  is the refractive index of the dielectric layer. The free-space propagation changes the position coordinate  $x$  with-

out affecting the direction coordinate  $p$ . With the use of generalized reduced angles, the interface transformation matrix is simplified and becomes the identity matrix.

Figures 5(a) and 5(b) show the transformation of the system PS representation when the photodetector is moved from the pixel aperture plane to the pixel floor, i.e., a surface photodetector versus a buried photodetector. Knowing the system PS representation of the buried photodetector on the pixel floor, where the photodetector physically limits the spatial dimensions of the PS representation, we can calculate a canonical PS for the buried photodetector pixel system. Here the canonical plane is located at the pixel aperture plane, and we obtain the canonical system PS by inverting the PS transformation that allowed us to propagate from the pixel aperture plane to the pixel floor [Figs. 5(b) and 5(c)]. The canonical system PS is then used in further calculations.

The paraxial formulas in the previous paragraph are included to provide an intuitive discussion. In general, however, we use nonparaxial formulas. These cannot be accurately modeled by using a cascade of ray transfer matrices, and their complexity quickly grows as the number of layers increases. The formulas for a single layer with index  $n$  and depth  $d$  are given by

$$x_o = x_i - d \frac{\frac{p_i}{n}}{\left[1 - \left(\frac{p_i}{n}\right)^2\right]^{1/2}}, \quad p_o = p_i. \quad (20)$$

The nonparaxial formulas reduce to those of the paraxial case for small angles. Note that in the nonparaxial case free-space propagation does not correspond to a pure shear. The nonparaxial formulas were used in all the calculations and figures in this paper.

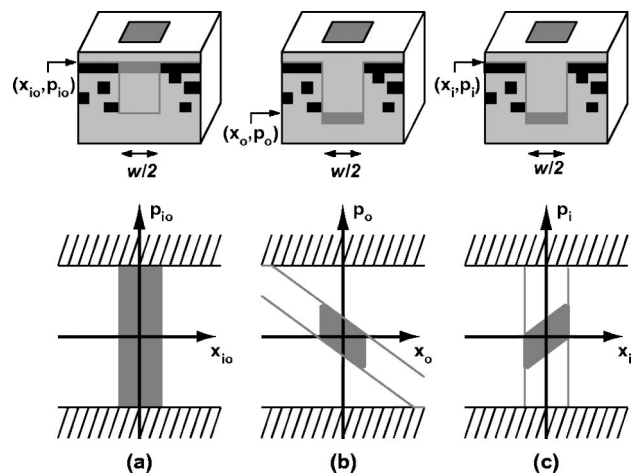


Fig. 5. PS representations of a pixel (50% fill factor): (a) pixel with surface photodetector, (b) pixel with buried photodetector [PS is given with respect to the photodetector plane  $(x_o, p_o)$ ], (c) pixel with buried photodetector. The input-referred PS is given with respect to the aperture plane  $(x_i, p_i)$ . In the pixel cross-sectional diagram, the light-shaded areas indicate  $\text{Si}_3\text{N}_4$ ,  $\text{SiO}_2$ , and  $\text{Si}$ , the black rectangles represent metal wires, and the dark-shaded rectangle represents the photodetector.

### 3. OPTICAL EFFICIENCY CALCULATION

We now show how to calculate the OE  $\eta_{\text{optical}}$  of a CMOS image sensor pixel, which typically has a buried photodetector. The calculation consists of two parts. First, we calculate a geometric efficiency  $\eta_{\text{geom}}$  by using the PS methods developed here. Second, we account for the transmission losses that occur in the dielectric tunnel by calculating a transmission efficiency  $\eta_{\text{trans}}$  using a scattering-matrix approach.<sup>21</sup> The geometric and transmission efficiencies are combined to yield the pixel OE.

#### A. Geometric Efficiency

The geometric efficiency  $\eta_{\text{geom}}$  includes the geometrical effects of the finite aperture size, the finite NA of the lens, and the bending of the light due to the different dielectric media in the tunnel. This geometric efficiency is calculated, using the PS approach, as

$$\eta_{\text{geom}} = \frac{G_{\text{detector}}}{G_{\text{aperture}}}, \quad (21)$$

where  $G_{\text{detector}}$  is the etendue captured by a buried photodetector and  $G_{\text{aperture}}$  is the etendue available at the aperture. We assume here that an on-axis pixel is located at the image plane of a lens that serves as the proximal source for the imaging sensor. The pixel aperture width is given by  $w/2$ , and its photodetector is buried a distance  $d$  from the aperture. For simplicity, we also assume that the buried photodetector is centered on the aperture and that their sizes are equal. The signal PS representation is therefore shown as the light-shaded area in Fig. 4(c). The system PS representation of the CMOS image sensor pixel with a buried photodetector is shown in Fig. 5(c), while the PS representation giving the acceptance range, and therefore the etendue of the pixel aperture, is shown in Fig. 5(a). We combine signal and system PS representations by intersecting the light-shaded area in Fig. 4(c) with the areas in Figs. 5(a) and 5(c), respectively (the insets in Fig. 9 below show the intersection). This yields the respective signal–system PS representations of the aperture and the detector, from which we determine the etendues. The geometric efficiency of the buried pixel is smaller than unity, while the efficiency of a surface pixel with equal aperture size is unity by definition.

The PS approach as described in the previous paragraph can also be used to calculate the geometric efficiency for off-axis pixels. In this case, the fan of rays is centered not on a chief ray perpendicular to the imaging plane but rather around an off-axis chief ray, whose angle depends on the location of the pixel in the image sensor. The signal PS representation shifts vertically, following a sinusoidal function of the angle of the chief ray (this variation is also seen in the insets in Fig. 9). While the pixel PS representation remains the same, the etendue of the signal–system PS representation formed by the intersection changes with off-axis chief ray angle.

#### B. Transmission Efficiency

An image sensor pixel, implemented in CCD or CMOS technology, includes alternating layers of dielectrics (transparent) and metals (opaque). The tunnel from the pixel aperture at the surface to the photodetector on the

pixel floor contains no metal; rather, the space is filled by a dielectric passivation layer ( $\text{Si}_3\text{N}_4$ ) and multiple dielectric insulation layers ( $\text{SiO}_2$ ) that separate the metal layers used for intrapixel interconnects. Even though the dielectric layers are transparent, they still have an effect on the likelihood of a photon reaching the photodetector, and OE calculations based on our PS approach have not included this effect so far. Hence we separately calculate the transmission efficiency by treating the tunnel as a dielectric stack of  $N$  layers, where each layer is characterized by its index of refraction and thickness.

The intuitive method of adding multiple reflected and transmitted waves quickly becomes awkward even for a few dielectric layers. Instead, we use the scattering-matrix approach<sup>21</sup> as described in Appendix A. This method uses the linear equations governing the propagation of light and the continuity of the tangential components of the light fields across an interface between two isotropic media. For simplicity, the scattering-matrix calculations assume that (1) each layer has a constant refractive index, (2) no light is scattered or absorbed by material imperfections within a layer, (3) the dielectric layers are infinite planes, which means that we do not model edge reflections *per se*, and (4) wavelength effects are ignored (i.e., we calculate transmission versus angle averaged uniformly over the visible wavelength band between 400 and 700 nm). A scattering matrix relates the intensity of a plane wave incident at the pixel aperture to the intensity of the corresponding plane wave incident at the photodetector plane. The ratio of these intensities, which in general depends on the angle of incidence of the plane wave, is plotted in Fig. 6 for a CMOS image sensor pixel with the shown geometry: The curve shows the average over all visible wavelengths. For a broad range of angles,  $\pm 30$  deg, the transmission efficiency is nearly constant at 0.73.

#### C. Optical Efficiency

To calculate the pixel OE, we must combine the geometric and transmission efficiencies. In our case, we observe that the transmission efficiency is a constant for all angles of interest and therefore a constant scaling factor

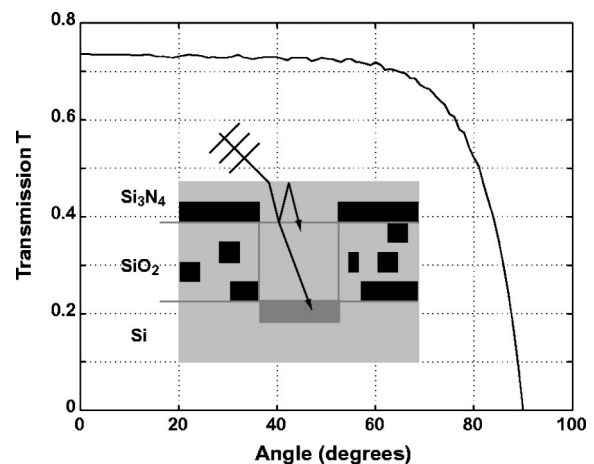


Fig. 6. Transmission efficiency of a CMOS image sensor pixel as a function of the angle of incidence of a plane wave calculated by using a scattering matrix approach. The curve represents the average transmission over visible wavelengths.

applied to the geometric efficiency. In other words, the pixel OE is simply the product of the geometric and transmission efficiencies.

#### 4. EXPERIMENTAL METHODS

The PS representations and transformations described in this paper involve a number of approximations, the most notable being the geometrical-optics approximation. We have performed two experiments to evaluate how well these PS calculations predict experimental measurements performed on a CMOS digital pixel sensor (DPS).<sup>5</sup> In addition, these experiments quantify how much the OE of CMOS image sensor pixels depends on (1) the 3D geometry of the pixel, i.e., size and location of photodetector, and (2) the location of the pixel within the image sensor situated behind the imaging lens. In a first experiment, we measured the averaged response from the pixels of a CMOS DPS illuminated by a quasi-plane wave whose angle was systematically varied. In a second experiment, we measured the responses from a collection of pixels of the same CMOS DPS placed behind a lens.

##### A. Plane-Wave Experiment

When the surface of the sensor is illuminated by quasi-plane waves without intervening optics, the resulting uniform irradiance yields a uniform pixel response subject to temporal read noise and spatial fixed pattern noise. By spatial and temporal averaging of the responses, we remove both noise contributions and obtain a very precise measure of how the angle of incidence influences the pixel response because of the 3D geometry of the pixel.

The experimental setup, shown in Fig. 7(a), included a stable white light source, a fiber light guide, a beam collimator, and the CMOS image sensor mounted on a rotation stage. Coupling the light from the light source into a fiber light guide followed by a beam collimator produced a uniform quasi-plane wave. The board with the sensor was vertically mounted on an XY-translation stage. The translation stage permitted the alignment of the center of the sensor with the rotation axis of the rotation stage. This made it possible to rotate the sensor while minimizing translation. Finally, a digital frame grabber captured the data from the sensor.

We confirmed the stability of the white light source before each experiment by comparing several frames taken at the same quasi-plane-wave irradiance and angle. We then set the source to generate a constant irradiance level at the pixel plane, and we fixed the integration time for the sensor throughout the experiment. We set the irradiance level high enough to minimize integration time, and thus the effect of dark current, while maintaining high signal-to-noise ratio. We then positioned the rotation stage to the desired angle and captured an image of the light field. To improve the precision of the measurement, we averaged the response of the center  $30 \times 30$  pixels. This measurement was repeated for different angles in both directions.

##### B. Imaging Experiment

The purpose of this experiment was to explore a more realistic image capture setting that includes an imaging

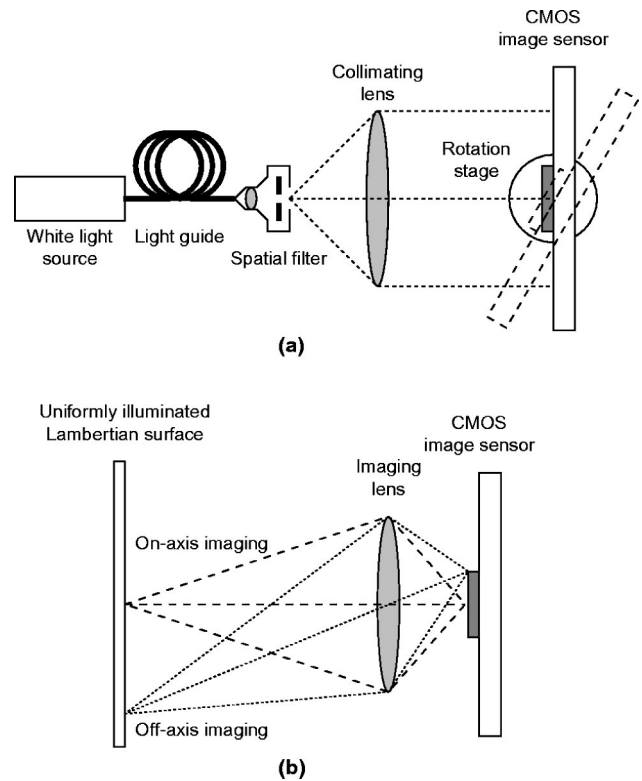


Fig. 7. Experimental setups: (a) plane-wave experiment, (b) imaging experiment.

lens. In this experiment, the illumination source is a large Lambertian source in the object plane filling the lens with light. The angle between the pixels and the chief ray coming from the exit pupil of the lens varied as a function of the pixel position within the sensor.

Figure 7(b) shows the setup, which consisted of a uniformly illuminated Lambertian surface, an  $f/1.8$  16-mm imaging lens providing a 23-deg full field of view (FOV), and the CMOS image sensor. In this experiment, variation with respect to angle was produced by the different positions of the pixels within the sensor.

Again, before the experiment, we confirmed the stability of the white light source by comparing several images taken at the same irradiance level. We set the irradiance level high enough to minimize integration time. We then acquired a set of ten images and averaged them to reduce any fluctuations due to temporal noise. The off-axis irradiance attenuation due to the  $\cos^4$  effect of the imaging lens is corrected for before analysis of the data.

#### 5. RESULTS

Figures 8 and 9 show the results from the two experiments. The horizontal axis in Fig. 8 measures the angle of the plane wave with respect to the sensor, and the vertical axis measures the attenuation of the signal with respect to on-axis presentation. Figure 9 shows the relative pixel response (measured across the center row) as the angle of the chief ray varies. The measurement error bars represent  $\pm 1$  standard error of the mean. The solid curves represent theoretical calculations using the

geometrical-optics PS approach. The error between the data and the model is summarized by the root mean square (rms) error,

$$\text{RMSE} = \left[ \frac{\sum_n (L_{\text{model}} - L_{\text{meas } n})^2}{N} \right]^{1/2}, \quad (22)$$

and by the maximum error,

$$E = \max_n \left( \left| \frac{L_{\text{model}} - L_{\text{meas } n}}{L_{\text{meas } n}} \right| \right). \quad (23)$$

In the rms error,  $N$  represents the number of measurements taken.

### A. Plane-Wave Experiment

The signals from off-axis pixels decrease regularly with the angle of incidence. The attenuation reaches 35% at a 23-deg angle, which corresponds to the typical FOV of a

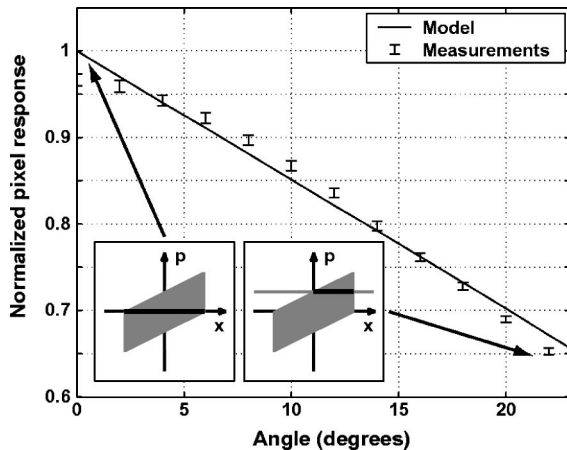


Fig. 8. Plane-wave experimental results: Pixel response, normalized with respect to on-axis pixel response, is plotted as a function of angle of incidence of a plane wave. The error bars and solid curve represent measured and predicted values, respectively.

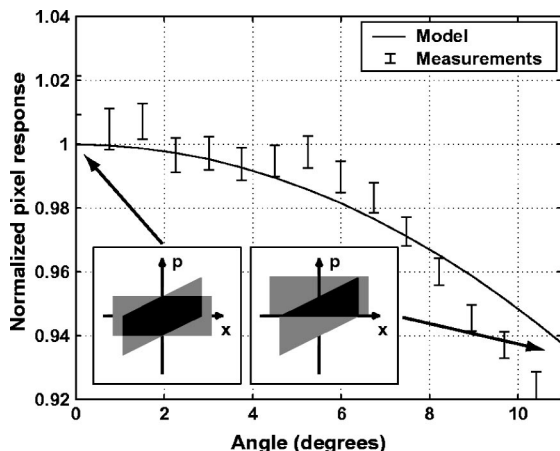


Fig. 9. Imaging experimental results: Pixel response, normalized with respect to on-axis pixel response, is shown as a function of angle of incidence of the chief ray from an  $f/1.8$  imaging lens with a 23-deg full FOV. The error bars and solid curve represent measured and predicted values, respectively.

single-lens-reflex camera standard objective. The attenuation observed in the buried pixel response is much larger than that which would be expected from simple  $\cos^4$  attenuation.<sup>7</sup> The pixel response is a result of the 3D geometry of the pixel. There is one free parameter when fitting the geometrical-optics PS model, i.e., the absolute on-axis pixel response. We have adjusted this parameter to minimize the rms error between the data points and the theory. The theory predicts the measured off-axis attenuation with a rms error of 0.01 and a maximum error of 0.03.

The two insets in Fig. 8 show the plane-wave PS (a horizontal line) superimposed on the buried photodetector PS for the two end points of the plot. When the plane wave is normally incident, the plane-wave PS falls along the  $x$  axis (corresponding to 0-deg incidence); and when the plane wave is incident at an oblique angle, the plane-wave PS shifts vertically, depending on the angle of incidence. The overlap between the pixel and plane-wave PS representations is used to predict the etendue and consequently the pixel response.

### B. Imaging Experiment

The attenuation of the normalized off-axis pixel response increases with the chief ray angle of the incident light cone. The attenuation reaches 6% at an 11-deg angle, which corresponds to the FOV of a telephoto lens with twice the focal length of that of a standard single-lens-reflex camera objective. This attenuation is once again far more pronounced than  $\cos^4$  attenuation and can only be attributed to the location of the photodetector in the pixel.<sup>7</sup> The geometrical-optics PS model, which incorporates the 3D pixel geometry, predicts the response reduction trend observed in the experiment with a rms error of 0.01 and a maximum error of 0.02.

Again, the two insets in Fig. 9 show the signal PS superimposed on the buried photodetector PS for the two end points of the plot. When the signal is normally incident, the rectangle representing the signal PS is centered on the  $x$  axis; when the signal is oblique, the signal PS shifts vertically along with the chief ray angle.

## 6. DISCUSSION

### A. Sensitivity, Functionality, and Technology Scaling

Geometrical-optics PS calculations permit the image sensor designer to evaluate pixel designs before building single-pixel test structures. Using the PS methods described here, the designer can analyze sensitivity–functionality trade-offs within and across CMOS process technology. For example, the PS model used to fit the data in Figs. 8 and 9 predicts that the on-axis pixel OE is reduced by 35% when the photodetector is moved from the pixel surface to the pixel floor, assuming an  $f/1.8$  imaging lens. In this section, we describe two additional cases in which design trade-offs can be examined.

First, consider the question of how a change in pixel circuitry might influence OE. Specifically, consider the choice between a typical active pixel sensor (APS)<sup>22</sup> and a

DPS.<sup>5</sup> The APS design is widely used, and within the pixel it includes only a light-sensitive photodetector, a reset transistor, an access transistor, and a source follower. The DPS is more complex and includes an analog-to-digital converter at each pixel. The early conversion from analog to digital form provides various advantages in speed<sup>23</sup> and high dynamic range.<sup>24</sup> However, the APS can be built by using only two metal layers, whereas the DPS needs at least four: Fewer metal layers decreases pixel depth and reduces vignetting.<sup>7</sup> Figure 10(a) shows the pixel OE as a function of the number of metal layers, assuming that an  $f/1.8$  imaging lens illuminates the pixel. Curves are shown for on-axis and off-axis pixels (at 11- and 23-deg FOV). For on-axis pixels, pixel response falls from 0.62 to 0.53. The off-axis (23-deg) response falls much more, from 0.38 down to 0.17. Hence the designer must evaluate whether these reductions in sensitivity are worth the increased functionality.

Second, the PS calculations make it possible to investigate how pixel OE is affected as CMOS process technology scales to smaller feature size. As the planar feature sizes scale, the metal interconnect layer thickness does not scale as much. Figure 10(b) shows how OE will change as technology scales. The curves are calculated assuming a two-layer metal APS pixel illuminated by an  $f/1.8$  imaging lens, and we further assume that the pixel size changes proportionately to technology so that the fill factor remains constant at 30%. Under these assumptions, shrinking the feature size increases the spatial sampling rate. However, as the curves for on-axis and off-axis pixels show, there is a significant loss in sensitivity due to vignetting. As technology scales from 0.35 to 0.18  $\mu\text{m}$ , the on-axis sensitivity changes from 0.67 to 0.62; meanwhile, the off-axis (23-deg) response changes from 0.52 to 0.38. Hence, again, the designer must evaluate whether the increased spatial sampling is worth the reduced sensitivity.

## B. Geometrical Optics Versus Wave Optics

As CMOS technology scales, the effects accounted for by wave optics, rather than pure geometrical optics, become

increasingly important. Over what range of CMOS technologies will the geometrical-optics PS approach provide a good approximation?

First, we have compared the geometrical- and wave-optics calculations by using parameters that correspond to the imaging experiment (Fig. 9, DPS, 0.35- $\mu\text{m}$  feature size, 5.5- $\mu\text{m}$  aperture width, 7.08- $\mu\text{m}$  tunnel depth). The wave-optics calculations are described in Appendix A; they include assumptions about imaging lens illumination, free-space propagation from the imaging lens to the photodetector, and diffraction effects at the lens and pixel apertures. We find that the off-axis attenuation predicted by using wave optics is within 2% of the empirical results (Fig. 11 corresponds to incident light with  $\lambda = 500$  nm). This is only slightly better than the geometrical-optics PS calculation and demonstrates that the two methods agree well.

The close agreement between geometrical- and wave-optics calculations depends on two factors: the wavelength of the incident light and the ratio of the pixel aperture width to the tunnel depth. First, wave-optics calculations are wavelength dependent and performed over the visible range from 400 to 700 nm, resulting in a 2%–3% difference. Second, the width–depth ratio is closely related to the Fresnel number  $F_N = (w/2)^2/(d\lambda)$ , which determines whether the wave field at the buried photodetector is in the near-field Fresnel or the far-field Fraunhofer regime. The near-field Fresnel numbers for the tunnel dimensions range from 3.9 ( $\lambda = 400$  nm) to 2.2 ( $\lambda = 700$  nm), confirming the Fresnel regime. Hence, for these wavelengths and pixel sizes, the geometrical-optics PS calculations are in close agreement with wave-optics calculations.

As CMOS technology scales to smaller feature sizes, smaller pixels and apertures become possible. However, pixel sizes will not necessarily scale at the same rate as that of CMOS technology: First, there is a lower limit on pixel size determined by the pixel light sensitivity and its capacity to hold charge; second, smaller pixels require increasingly expensive well-corrected optics. For quite-

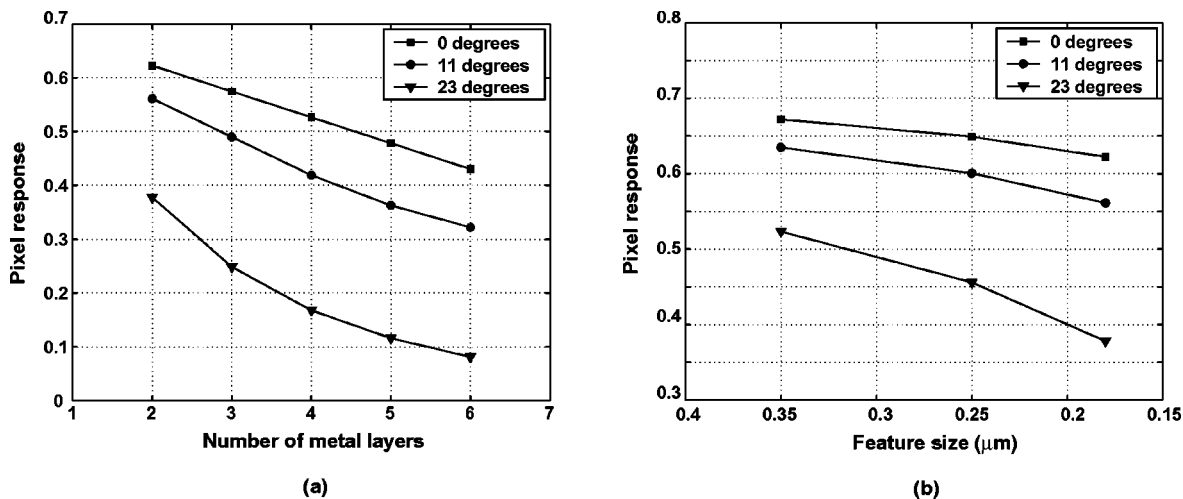


Fig. 10. OE predictions based on geometrical-optics PS. (a) On-axis pixel response ( $f/1.8$  imaging lens) is shown as a function of number of metal layers in a 0.18- $\mu\text{m}$  standard CMOS process. Aperture width is equal to 1.92  $\mu\text{m}$ , and tunnel depths vary from 3.73 to 9.05  $\mu\text{m}$ . (b) On-axis pixel response for a standard APS pixel with a 30% fill factor using two metal layers as a function of feature size of the CMOS technology used. Aperture width and tunnel depth vary from 3.72 to 1.92  $\mu\text{m}$  and from 4.37 to 3.73  $\mu\text{m}$ , respectively.

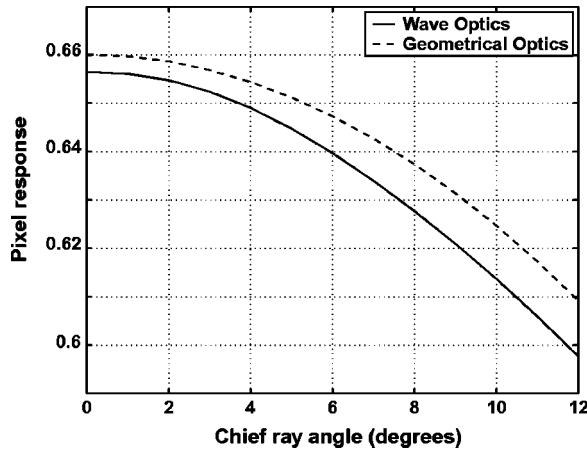


Fig. 11. Comparison of geometrical-optics PS and wave-optics approaches to calculating pixel OE as a function of angle of incidence of the chief ray of an  $f/1.8$  imaging lens with a full FOV of 23 deg. The computed pixel OE includes both geometric and transmission efficiency. When these theoretical curves are plotted with the data in Fig. 9, both the theory and the data are normalized to the on-axis pixel OE, effectively removing the transmission loss.

small pixel sizes, at the limit of what we anticipate as being practical, deviations between the two calculations remain in reasonable agreement. For example, consider a two-layer metal APS pixel (0.18- $\mu\text{m}$  feature size, 1.92- $\mu\text{m}$  aperture width, 3.73- $\mu\text{m}$  tunnel depth). In that case, the difference between geometrical- and wave-optics calculations is less than 9%. We therefore expect the geometrical-optics PS approach to remain a good approximation to wave-optics calculations. Hence it will remain a valuable tool to predict the OE of CMOS image sensor pixels even as CMOS technology scales.

## APPENDIX A

### 1. Scattering-Matrix Formalism

The intuitive method of adding multiple reflected and transmitted waves becomes quickly impractical even for a few dielectric layers. A more elegant approach that employs  $2 \times 2$  matrices, referred to as the scattering-matrix approach, will now be discussed. This method, pioneered by Abelès,<sup>25,26</sup> is based on the fact that the equations that govern the propagation of light are linear and that continuity of the tangential components of the light fields across an interface between two isotropic media can be regarded as a  $2 \times 2$  linear matrix transformation. The present development is due to Hayfield and White.<sup>21</sup>

Consider a stratified medium that consists of a stack of  $m$  parallel layers sandwiched between two semi-infinite ambient (0) and substrate ( $m + 1$ ) media. Let all media be linear homogeneous and isotropic, let the complex index of refraction and the thickness of the  $j$ th layer be  $n_j$  and  $d_j$ , respectively, and let  $n_0$  and  $n_{m+1}$  represent the complex indices of refraction of the ambient and substrate media. A monochromatic plane wave incident on the parallel layers, originating from the ambient, generates a resultant transmitted plane wave in the substrate. We are now interested in determining the amplitude of the resultant wave. The total field inside the  $j$ th layer, which is excited by the incident plane wave, consists of two

plane waves: a forward-traveling and a backward-traveling plane wave with complex amplitudes  $E^+$  and  $E^-$ , respectively.

The total field in a plane  $z$ , parallel to the boundary, can be described by a  $2 \times 1$  column vector:

$$\mathbf{E}(z) = \begin{pmatrix} E^+(z) \\ E^-(z) \end{pmatrix}. \quad (\text{A1})$$

If we consider the fields at two different planes  $z'$  and  $z''$ , by virtue of linearity,  $\mathbf{E}(z')$  and  $\mathbf{E}(z'')$  are related by a  $2 \times 2$  matrix transformation:

$$\begin{pmatrix} E^+(z') \\ E^-(z') \end{pmatrix} = \begin{bmatrix} S_{11} & S_{12} \\ S_{21} & S_{22} \end{bmatrix} \begin{pmatrix} E^+(z'') \\ E^-(z'') \end{pmatrix}. \quad (\text{A2})$$

The  $2 \times 2$  matrix defined by the planes immediately adjacent to the 01 and  $m(m + 1)$  interfaces is called the scattering matrix  $\mathbf{S}$ . The scattering matrix represents the overall reflection and transmission properties of the stratified structure and can be expressed as a product of interface and layer matrices  $\mathbf{I}$  and  $\mathbf{L}$  that describe the entire stratified structure:

$$\mathbf{S} = \mathbf{I}_{01} \mathbf{L}_1 \cdots \mathbf{I}_{(j-1)j} \mathbf{L}_j \cdots \mathbf{L}_m \mathbf{I}_{m(m+1)}. \quad (\text{A3})$$

The matrix  $\mathbf{I}$  of an interface between two media relates the fields on both its sides by using Fresnel's reflection and transmission coefficients for the interface:

$$\mathbf{I}_{(j-1)j} = [1/t_{(j-1)j}] \begin{bmatrix} 1 & r_{(j-1)j} \\ r_{(j-1)j} & 1 \end{bmatrix}. \quad (\text{A4})$$

The interface Fresnel transmission and reflection coefficients  $t_{(j-1)j}$  and  $r_{(j-1)j}$  are evaluated by using the complex indices of refraction of the two media that define the interface and the local angle of incidence by repeated application of Snell's law:

$$n_0 \sin \theta_0 = \cdots = n_j \sin \theta_j = \cdots = n_{m+1} \sin \theta_{m+1}. \quad (\text{A5})$$

The formulas to compute the Fresnel coefficients can be found in many optics textbooks<sup>27</sup>; the complex indices of refraction are dependent on the material used in the CMOS process. We now turn our attention to the effect of propagation through a homogeneous layer of index of refraction  $n_j$  and thickness  $d_j$ . The layer matrix  $\mathbf{L}$  can be written as

$$\mathbf{L}_j = \begin{bmatrix} \exp(j\beta_j) & 0 \\ 0 & \exp(-j\beta_j) \end{bmatrix}, \quad (\text{A6})$$

where the layer phase thickness  $\beta_j$  is given by

$$\beta_j = \frac{2\pi}{\lambda} d_j n_j \cos \theta_j. \quad (\text{A7})$$

The overall reflection ( $R$ ) and transmission ( $T$ ) coefficients of the stratified structure are

$$R = \frac{S_{21}}{S_{11}}, \quad (\text{A8})$$

$$T = \frac{1}{S_{21}}. \quad (\text{A9})$$

We use these formulas to calculate the overall transmission efficiency of the dielectric tunnel from the pixel aperture at the surface to the photodetector on the pixel floor by treating the tunnel as a dielectric stack of  $N$  layers. In the case of a DPS in 0.35- $\mu\text{m}$  CMOS technology, there are six layers with refractive indices varying from 1.48 to 3.44 and thicknesses ranging from 1 to 1.67  $\mu\text{m}$ . We perform the calculation for a wide range of angles of incidence and do this for every wavelength in the visible wavelength band between 400 and 700 nm. We then average the angle dependency over all wavelengths to produce the transmission efficiency plot in Fig. 6. We note that most of the transmission losses occur at the initial air-Si<sub>3</sub>N<sub>4</sub> interface and the final SiO<sub>2</sub>-Si interface with minor losses at the intermediate interfaces.

## 2. Wave-Optics Calculation

We describe in this paper an intuitive geometrical-optics PS model to calculate the OE of image sensor pixels. This description can be extended to include wave-optics phenomena, such as diffraction, interference, coherence, and polarization. However, this requires a six-dimensional coordinate frame  $(x, y, p, q, t, \omega)$  and leads to a computationally more intensive PS representation based on the Wigner transform.<sup>14,15</sup> Instead, we opted for a comparison of the geometrical-optics PS prediction of the OE with a straightforward wave-optics prediction. This allows us to evaluate the effect of diffraction at the lens rim and at the finite pixel aperture on the OE. We showed that the two predictions are very similar. In this section, we describe the steps used in calculating the OE of a pixel at the image plane of a lens within the wave-optics framework.

Consider an imaging system consisting of an imaging lens with a finite aperture diameter, illuminated by a set of plane waves. The plane waves are imaged onto a sensor plane containing a pixel of finite aperture size and a buried photodetector. Assume that (1) we model incoherent imaging, (2) we perform the calculations for the visible range of wavelengths from 400 to 700 nm, (3) we use both the paraxial Fresnel propagation kernel and a nonparaxial wide-angle kernel when performing free-space propagation from object plane to lens plane and from lens plane to imaging plane, and (4) we include the effect of evanescent waves.

The optical wave field defined at the object plane,  $U_o(x, y, 0)$ , is converted into its angular spectrum:

$$A_o\left(\frac{\alpha}{\lambda}, \frac{\beta}{\lambda}; 0\right) = \int_{-\infty}^{\infty} \int_{-\infty}^{\infty} U_o(x, y, 0) \times \exp\left[-j2\pi\left(\frac{\alpha}{\lambda}x + \frac{\beta}{\lambda}y\right)\right] dx dy. \quad (\text{A10})$$

It is propagated over the free-space object distance  $z_o$  by using paraxial propagation kernels, leading to

$$A_o\left(\frac{\alpha}{\lambda}, \frac{\beta}{\lambda}; z_o\right) = A_o\left(\frac{\alpha}{\lambda}, \frac{\beta}{\lambda}; 0\right) \exp\left(j\frac{2\pi}{\lambda}z_o\right) \times \exp\left[-j\pi\lambda z_o\left[\left(\frac{\alpha}{\lambda}\right)^2 + \left(\frac{\beta}{\lambda}\right)^2\right]\right], \quad (\text{A11})$$

or nonparaxial propagation kernels, leading to

$$A_o\left(\frac{\alpha}{\lambda}, \frac{\beta}{\lambda}; z_o\right) = A_o\left(\frac{\alpha}{\lambda}, \frac{\beta}{\lambda}; 0\right) \times \exp\left[j\frac{2\pi}{\lambda}(1 - \alpha^2 - \beta^2)^{1/2}z_o\right]. \quad (\text{A12})$$

At the plane of the imaging lens, we convert the incident spectrum back into a wave field, given by

$$U_o(x, y, z_o) = \int_{-\infty}^{\infty} \int_{-\infty}^{\infty} A_o\left(\frac{\alpha}{\lambda}, \frac{\beta}{\lambda}; z_o\right) \times \exp\left[j2\pi\left(\frac{\alpha}{\lambda}x + \frac{\beta}{\lambda}y\right)\right] d\frac{\alpha}{\lambda} d\frac{\beta}{\lambda}, \quad (\text{A13})$$

to allow for interaction with the phase and amplitude distribution of the lens, i.e., a quadratic phase factor and a finite aperture defined by the pupil function  $P(x, y)$ , yielding

$$U_l(x, y, z_o) = P(x, y) \exp\left[j\frac{k}{2f}(x^2 + y^2)\right] U_o(x, y, z_o). \quad (\text{A14})$$

The transmitted field  $U_l(x, y, z_o)$  is then again converted into its angular spectrum  $A_l(\alpha/\lambda, \beta/\lambda; z_o)$  as shown above and propagated over the free-space imaging distance  $z_i$  to yield  $A_i(\alpha/\lambda, \beta/\lambda; z_o + z_i)$ . At the imaging plane, the field  $U_i(x, y, z_o + z_i)$  interacts with the aperture of the pixel  $t_p(x, y)$ , and the resulting field  $U_p(x, y, z_o + z_i) = t_p(x, y)U_l(x, y, z_o + z_i)$  is once more converted and propagated over the pixel depth  $d$  before reaching the photodetector where it is collected  $U_p(x, y, z_o + z_i + d)$ . We compare the energy contained within the field incident on the pixel area,  $U_p(x, y, z_o + z_i)$ , with the energy contained within the field incident on the photodetector area,  $U_p(x, y, z_o + z_i + d)$ , by integration of the respective fields over the respective areas of the pixel aperture and the photodetector. The OE is here defined as the ratio of these integrals.

## ACKNOWLEDGMENTS

This work is supported by the Programmable Digital Camera project, by Agilent Technologies, and by Philips Semiconductors. P. B. Catrysse is "Aspirant" with the Fund for Scientific Research-Flanders (Belgium). We thank A. El Gamal, R. Byer, H. Thienpont, I. Veretennicoff, B. Fowler, R. Piestun, J. DiCarlo, Y. Takashima, and F. Xiao for valuable discussions and helpful comments.

Address correspondence to Peter B. Catrysse (c/o Wandell Lab), Jordan Hall, Building 420, Room 490, Stanford University, Stanford, California 94305-2130. Phone, 650-725-1255; fax, 650-723-0993; e-mail, peter@kaos.stanford.edu.

## REFERENCES

- J. R. Janesick, K. Evans, and T. Elliot, "Charge-coupled-device response to electron beam energies of less than 1 keV up to 20 keV," *Opt. Eng.* **26**, 686–691 (1987).
- B. Fowler, A. El Gamal, D. Yang, and H. Tian, "A method for estimating quantum efficiency for CMOS image sensors," in *Solid State Sensor Arrays: Development and Applications II*, M. M. Blouke, ed., Proc. SPIE **3301**, 178–185 (1998).
- D. Yang, H. Tian, B. Fowler, X. Liu, and A. El Gamal, "Characterization of CMOS image sensors with Nyquist rate pixel level ADC," in *Sensors, Cameras, and Applications for Digital Photography*, N. Sampat and T. Yeh, eds., Proc. SPIE **3650**, 52–62 (1999).
- J. Giest and H. Baltes, "High accuracy modeling of photodiode quantum efficiency," *Appl. Opt.* **28**, 3929–3938 (1989).
- D. Yang, A. El Gamal, B. Fowler, and H. Tian, "A  $640 \times 512$  CMOS image sensor with ultrawide dynamic range floating-point pixel-level ADC," *IEEE J. Solid-State Circuits* **34**, 1821–1834 (1999).
- J. A. Penkethman, "Calibrations and idiosyncrasies of micro-lensed CCD cameras," in *Current Developments in Optical Design and Optical Engineering VIII*, R. E. Fischer and W. J. Smith, eds., Proc. SPIE **3779**, 241–249 (1999).
- P. Catrysse, X. Liu, and A. El Gamal, "QE reduction due to pixel vignetting in CMOS image sensors," in *Sensors and Camera Systems for Scientific, Industrial, and Digital Photography Applications*, M. M. Blouke, N. Sampat, G. M. Williams, Jr., and T. Yeh, eds., Proc. SPIE **3965**, 420–430 (2000).
- Luminous, Silvaco International, Santa Clara, Calif., 1995.
- Medici, Avanti Corporation, Fremont, Calif., 1998.
- M. Hideki, "Simulation for 3-D optical and electrical analysis of CCD," *IEEE Trans. Electron Devices* **44**, 1604–1610 (1997).
- R. J. Pegis, "The modern development of Hamiltonian optics," in *Progress in Optics I*, E. Wolf, ed. (North-Holland, Amsterdam, 1961), pp. 1–29.
- R. Winston, "Light collection within the framework of geometrical optics," *J. Opt. Soc. Am.* **60**, 245–247 (1970).
- J. W. Goodman, *Introduction to Fourier Optics*, 2nd ed. (McGraw-Hill, San Francisco, Calif., 1996), p. 404.
- M. J. Bastiaans, "Wigner distribution function and its application to first-order optics," *J. Opt. Soc. Am.* **69**, 1710–1716 (1979).
- D. Dragoman, "The Wigner distribution function in optics and optoelectronics," in *Progress in Optics XXXVII*, E. Wolf, ed. (Elsevier Science, Amsterdam, 1997), pp. 1–56.
- A. Walther, "Gabor's theorem and energy transfer through lenses," *J. Opt. Soc. Am.* **57**, 639–644 (1967).
- R. N. Bracewell, *The Fourier Transform and Its Applications*, 2nd ed. (McGraw-Hill, New York, 1986), p. 52.
- W. H. Steel, "Luminosity, throughput, or etendue," *Appl. Opt.* **13**, 704–705 (1974).
- A. A. Lohmann, R. G. Dorsch, D. Mendlovic, Z. Zalevsky, and C. Ferreira, "Space-bandwidth product of optical signals and systems," *J. Opt. Soc. Am. A* **13**, 470–473 (1996).
- M. J. Bastiaans, "The Wigner distribution function applied to optical signals and systems," *Opt. Commun.* **25**, 26–30 (1978).
- P. C. S. Hayfield and G. W. T. White, "An assessment of the suitability of the Drude-Tronstad polarized light method for the study of film growth on polycrystalline metals," in *Ellipsometry in the Measurement of Surfaces and Thin Films*, N. M. Bashara, A. B. Buckman, and A. C. Hall, eds. (National Bureau of Standards, Washington, D.C., 1964), Vol. 256, pp. 157–200.
- E. R. Fossum, "Active pixel sensors: are CCD's dinosaurs?" in *Charge-Coupled Devices and Solid State Optical Sensors III*, M. M. Blouke, ed., Proc. SPIE **1900**, 2–14 (1993).
- S. Kleinfelder, S. Lim, X. Liu, and A. El Gamal, "A 10kframes/s  $0.18\mu\text{m}$  CMOS digital pixel sensor with pixel-level memory," in *2001 International Solid-State Circuits Conference—Digest of Technical Papers* (IEEE Press, Piscataway, N.J., 2001), pp. 88–89.
- B. Wandell, P. Catrysse, J. DiCarlo, D. Yang, and A. El Gamal, "Multiple capture single image architecture with a CMOS sensor," in *Proceedings of the International Symposium on Multispectral Imaging and Color Reproduction for Digital Archives* (Society of Multispectral Imaging of Japan, Chiba, Japan, 1999), pp. 11–17.
- F. Abelès, "Recherches sur la propagation des ondes électromagnétiques sinusoidales dans les milieux stratifiés: application aux couches minces," *Ann. Phys. (Paris)* **5**, 596–640 (1950).
- F. Abelès, "Recherches sur la propagation des ondes électromagnétiques sinusoidales dans les milieux stratifiés: application aux couches minces," *Ann. Phys. (Paris)* **5**, 706–782 (1950).
- M. Born and E. Wolf, *Principles of Optics*, 6th (corrected) ed. (Pergamon, Oxford, UK, 1980), pp. 38–41.